Carbon 238 (2025) 120259

Contents lists available at ScienceDirect

Carbon

journal homepage: www.elsevier.com/locate/carbon

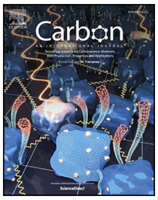

Understanding the effect of transport phenomena in deep-injection floating catalyst chemical vapor deposition carbon nanotube synthesis

Muxiao Li [a,1], Jui Junnarkar [b,1], Arthur W.N. Sloan [b,c,1], Eldar Khabushev [b], Ana Victoria Benavides-Figueroa [a], Mingrui L. Gong [b], Miguel Garza [b], Joe F. Khoury [b], Davide Cavuto [b], Steven M. Williams [b], Daniele Micale [d], Mauro Bracconi [d], Matteo Maestri [d], Glen C. Irvin Jr. [b], Matteo Pasquali [a,b,e,f,g,*]

[a] *Department of Chemistry, William Marsh Rice University, Houston, TX, 77005, United States*
[b] *Department of Chemical and Biomolecular Engineering, William Marsh Rice University, Houston, TX, 77005, United States*
[c] *Materials and Manufacturing Directorate, Air Force Research Laboratory, Wright-Patterson Air Force Base, 45433, OH, United States*
[d] *Laboratory of Catalysis and Catalytic Processes, Dipartimento di Energia, Politecnico di Milano, Via La Masa 34, Milano, Italy*
[e] *Department of Materials Science and Nanoengineering, William Marsh Rice University, Houston, TX, 77005, United States*
[f] *The Smalley-Curl Institute, William Marsh Rice University, Houston, TX, 77005, United States*
[g] *The Carbon Hub, William Marsh Rice University, Houston, TX, 77005, United States*

ARTICLE INFO

Keywords:
Carbon nanotubes
Floating-catalyst chemical vapor deposition
Deep-injection
Computational fluid dynamics
Methane pyrolysis

ABSTRACT

We explore deep injection (DI) floating catalyst chemical vapor deposition (FCCVD) for carbon nanotube (CNT) growth, focusing on momentum and heat transport effects. By systematically changing process gas composition, we study the effects of gas physical properties on reactor productivity while preserving other process parameters. DI causes a colder jet to penetrate deep into the reactor, creating an axial recirculation near the reactor walls. We find nitrogen and argon are interchangeable due to similar transport properties. Increasing the helium fraction in the process gas lowers jet momentum, reducing its length and recirculation size; beyond a certain level, the changes in reactor flow pattern cause a productivity drop. Increasing hydrogen fraction affects the flow and thermal profiles similarly; but productivity decreased further due to the chemical effects of hydrogen, preventing the formation of active species. Computational fluid dynamics simulations suggest that high productivity of DI reactor is associated with the colder jet meeting hotter recirculating gases, creating local conditions for catalyst formation in the presence of activated carbon precursors at the jet/recirculation interface. Under optimum conditions, we achieve ~13 % methane conversion, >90 % CNT selectivity, and ~430 mg/h productivity, among the highest results reported so far. This work provides valuable insights for designing efficient CNT reactors.

1. Introduction

Carbon nanotubes (CNTs) are a class of promising nanomaterials with unique properties [1,2], which could find use in numerous industrial applications if efficiently produced at large scale and with quality. Currently, the floating catalyst chemical vapor deposition (FCCVD) method is considered the most technologically viable approach for industrial-scale production of high-quality few-walled CNTs (FWCNTs) because it enables continuous CNT growth without substrates, has great potential for scalability, and requires minimal post-synthesis purification [2]. Moreover, the FCCVD process yields high-quality CNTs suitable to fabricate macroscopic CNT materials such as direct-spun and solution-processed fibers [3–7], films [8–12] and foams [13]. However, FCCVD reactor designs and processes are still at an early point in development due to the incomplete understanding of reaction mechanisms and reactor flow phenomena, which yields inefficient use of the reactor volume and bottlenecks in production rates [14]. Current industrial scale production of FWCNTs is limited to a few producers worldwide (OCSiAl, Meijo Nano Carbon, Huntsman Corporation, Tortech Nano Fibers), operating reactors with 1–100 ton/year capacity [15]. Most academic FCCVD reports show process feedstock conversion to solid carbon of less than 1 % and high dilution of carbon feedstock

---

[*] Corresponding author. Department of Chemical and Biomolecular Engineering, William Marsh Rice University, Houston, TX, 77005, United States.
E-mail address: mp@rice.edu (M. Pasquali).

[1] These authors contributed equally to this work.

https://doi.org/10.1016/j.carbon.2025.120259
Received 19 December 2024; Received in revised form 13 March 2025; Accepted 26 March 2025

with hydrogen or inert gases, clearly not suitable for commercial adoption [16], and likely lagging behind the industrial state-of-the-art [17].

FCCVD involves the decomposition of carbon feedstock (typically hydrocarbon) over metal nanoparticles, usually formed *in situ*, acting as both a catalyst and a template for the growing CNTs. A commonly accepted but simplified reaction mechanism [18–20] states that CNT growth takes place when two conditions are simultaneously satisfied: catalyst nanoparticles of the correct size (one to few nanometers) [20,21] are formed and a sufficient feed rate of reactive carbon species is supplied. In other words, CNT growth requires synchronization of catalyst particle formation with carbon feedstock activation to avoid catalyst overgrowth or early deactivation. The synchronization of the processes is complicated by the coupling of catalyst aerosol dynamics and feedstock decomposition kinetics with non-uniform temperature profiles and complex flow patterns of gases inside the reactor. The way these processes interplay is specific to individual reactor configurations and operating conditions, and their idiosyncratic nature has been a major challenge to the intensification of FCCVD processes over the past two decades. As a result, FCCVD exhibits low catalyst utilization (only a small amount of injected catalyst participates in growing CNTs), high carbon feedstock dilution, and low conversion of carbon feedstock when high-quality product is required.

In 2021, Lee et al. [22] reported that some FCCVD limitations could be overcome to simultaneously achieve higher reaction productivity and CNT quality. The authors recapitulate the importance of gas recirculation previously identified [23] in a high temperature gradient of classical FCCVD reactors, observed both upstream and downstream of reactor hot zone. They suggested that injecting the gas mixture (reacting gases, process gas, and catalyst precursors) directly into the hot zone beyond the inlet recirculation zone via a long, narrow injection cannula, could help prevent catalyst trapping in the upstream recirculating vortices. Preventing this catalyst trapping helps maintain a small size of catalyst particles, which is essential for FWCNT synthesis. Unlike the more common near-unidirectional Poiseuille-like flows in FCCVD reactors [19,24], deep-injection causes a high-velocity jet to move through the center of the reactor tube, which drives more complex flow and temperature patterns within the main body of the reactor, where CNT growth occurs. Thus, we expect gas physical properties (density, thermal conductivity, etc.) should significantly affect flow patterns and CNT growth, in general. Although earlier work has considered various process gases [25], to our knowledge the effects of gas mixture physical properties on reaction performance have not been investigated systematically.

Here, we study the effect of transport phenomena within a deep-injection FCCVD reactor via a systematic selection of process gas (gas besides feedstock) compositions. We show that, for efficient CNT synthesis, the mixture of gases exiting the cannula must have sufficient momentum (i.e., a sufficiently high Reynolds number) to drive a large recirculation in the main reactor body (hot zone), which brings hot gases to the reactor front via recirculation along the reactor walls. We also show that the radiative coupling of the injection cannula to the reactor walls is important, providing efficient pre-heating to the process gases. We infer that the CNT growth happens where the hotter recirculating gases, containing activated carbon species, meet the colder freshly injected gases, containing catalyst.

2. Materials and methods

2.1. Synthesis of CNTs by FCCVD

A horizontal three-zone electrically-heated furnace equipped with a mullite tube (length of 1.36 m with an inner diameter of 6.35 cm) was used to synthesize CNTs. The furnace wall temperature was set to 1200 °C in all zones. Methane was the carbon feedstock and was introduced at 117 SCCM (hereinafter, 25 °C and 1 atm reference condition). In the baseline recipe, two process gases were introduced together with methane: hydrogen (1702 SCCM) and argon (2844 SCCM). A portion of the total argon flow rate (1461 SCCM) was used as a carrier gas for catalyst precursors delivery consisting of 1457 SCCM for ferrocene and 4 SCCM for thiophene. All gas flow rates were controlled by MC Series Alicat mass flow controllers providing 0.5 % reading accuracy. Ferrocene was delivered into the reactor via sublimation (bath temperature: 57 °C) and thiophene via a bubbler evaporator (bath temperature: −6 °C) at near ambient pressure of 103.4 kPa. The estimated average residence time in the hot zone was 7.5 s (detailed calculation can be found in supplementary information). An alumina injection tube with an ID of 4.78 mm and wall thickness of 0.78 mm was utilized with an injection depth of 18 cm from the reactor tube front end, optimized for the baseline recipe. Details of the experimental parameters in the baseline recipe are summarized in Table 1 and a schematic of the experimental setup can be found in Fig. 1.

The optimal recipe yields ~430 mg/h (7.17 mg/min) of CNTs (quantified after purification), or 1.53 mg/L productivity when normalized by the total gas normal flow rate (4.663 SLPM), with 13.0 % conversion of methane into solid carbon, 96.4 % CNT selectivity (carbon), 4.7 % residual iron and CNT aspect ratio (ratio of length to diameter) of ~7000 (see below for the definition of the reactor and product metrics). For comparison, a 6.1 % conversion at 1.88 mg/L productivity (6 mg/min at 3200 SCCM) was reported by Lee et al. [22]; Zhang et al. [12] reported higher conversion (up to 25 %) but did not report productivity. Note that the optimized HiPco reactor typically produced ~1 g/h at a gas flow rate of ~500 SLPM, i.e., HiPco had a conversion of 0.007 % and productivity of about 0.033 mg/L.

To better understand the effects of process gas on the CNT growth, we controlled the process gas composition by replacing argon (Ar) in the baseline recipe with nitrogen (N_2), helium (He), or hydrogen (H_2) (denoted as substituting gases hereinafter). For consistency, we maintained the same total gas flow rate (to maintain the same approximate residence time), methane (CH_4) flow rate, and delivery rates of ferrocene and thiophene (by maintaining the same sublimation/evaporation conditions (carrier gas flow rate, temperature and pressure) of the catalyst precursors); where necessary, we changed carrier gas type, as described in section 3.3. The molar fraction of each gas species at conditions covered in this study is shown in Table 2, and specific gas flow rates in each test of the study are found in SI Table S1. To ensure minimum effect of impurities on the synthesis process, we utilized Ultra High Purity grade gases from Airgas (99.999 % for Ar, N_2, He, H_2 and 99.99 % for CH_4).

2.2. CNT characterization

We utilize a previously published purification process to remove

Table 1
Experimental parameters in the baseline conditions.

Baseline Reaction Conditions			
Reactor size (cm)	Inner diameter 6.35	Hot zone length 91.4	
Reactor temperature (°C)	1200		
Reactor orientation	Horizontal		
Reactor tube material	Mullite		
Gas flow rate (SCCM)	CH_4	H_2	Ar
Total gas flow rate: 4663 SCCM	117	1702	2844
H_2/CH_4 input molar ratio	14.5		
Residence time in the hot zone (s)	7.5		
Target catalyst precursor and growth promoter flow rate (mg/h)	Ferrocene	Thiophene	
Target S/Fe input molar ratio: 0.27	130	16.1	
Injection tube material	Alumina		
Injection tube ID (mm)	4.78		
Injection depth (cm)	18		

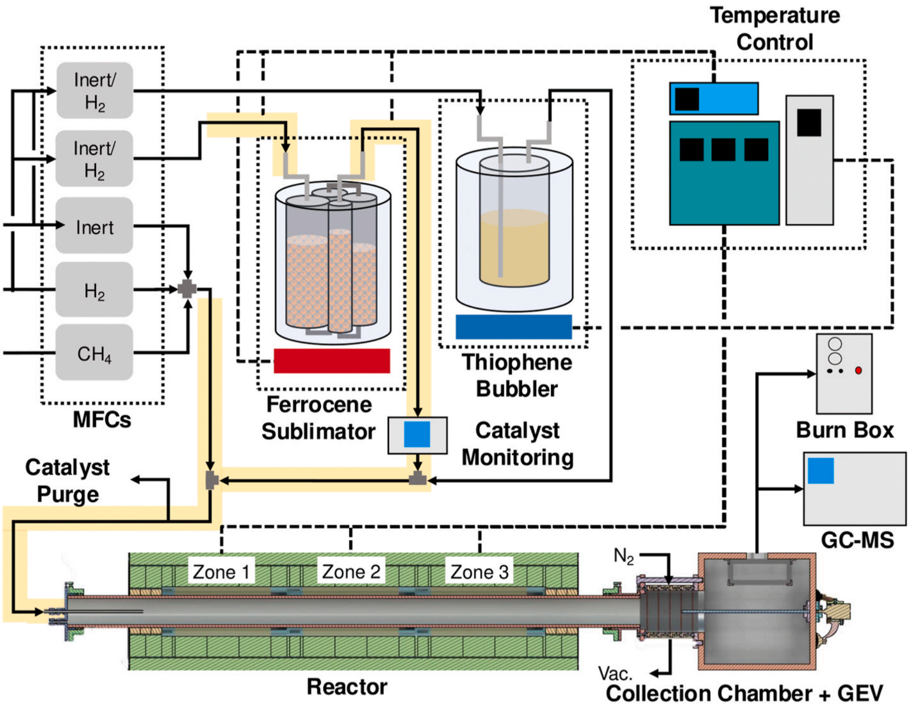

Fig. 1. Schematic of FCCVD CNT synthesis reactor. Yellow shaded process lines are heated to prevent ferrocene condensation. (For interpretation of the references to color in this figure legend, the reader is referred to the Web version of this article.)

Table 2

Experimental gas compositions using Ar, N_2, He, H_2, and their combinations as process gases. Numbers in paratheses refer to using N_2/He/H_2 as catalyst carrier instead of Ar.

Tested Conditions	Ar (baseline recipe)	N_2	He	H_2
Gas content (mol%)				
CH_4	2.5			
x of H_2	36.5			46.5; 56.5; 66.2; (67.8); 97.5
Ar	61.0	61.0-y		97.5-x
y of inert gas	0	29.7; (31.3); 61.0	10.0; 15.0; 20.0; 29.7; (31.3); 55.0; 61.0	0

carbon impurities and residual catalyst via air oxidation followed by a concentrated hydrochloric acid wash [26–28]. The purification is optimized to yield CNTs that can be dissolved in strong acids and converted into fibers via solution spinning, or "spinnable CNTs" [29]. The mass changes at the first purification step are used to calculate the fraction of spinnable CNTs (hereafter just CNT); residual catalyst is calculated via the second purification step (we find that this value is consistent with the thermogravimetric analysis, see SI). Details of the standard purification method and composition calculation are reported in the SI.

The conversion of CH_4 to solid carbon (Equation (1)) and the CNT selectivity (Equation (2)) can be derived from these sample composition values. The mass of output solid carbon is obtained by subtracting the catalyst mass measured via TGA and acid wash from the mass of collected material.

$$\mathrm{CH_4\ to\ solid\ carbon\ conversion\ (\%)} = \frac{\mathrm{Mass\ of\ \ solid\ carbon}}{\mathrm{Mass\ of\ carbon\ from\ input\ CH_4}} \tag{1}$$

$$\mathrm{CNT\ selectivity\ (\%)} = \frac{\mathrm{Mass\ of\ CNTs}}{\mathrm{Mass\ of\ output\ solid\ carbon}} \tag{2}$$

Thus, the mass of CNTs per mass input of carbon can be defined as the product of conversion and selectivity.

We also apply thermogravimetric Analysis (TGA) using Mettler Toledo TGA/DSC 3+ to quantify the composition of iron residual in as-produced samples. The ramp conditions and TG curves are included in SI (Fig. S1). We collect the residual iron in weight percentage assuming the remaining product after the ramp is Fe_2O_3. The remaining mass (%) curve as a function of ramp temperature with iron residual noted for key growth conditions (0 %, 30 %, 61 % of substitution process gas N_2/He/H_2) can also be found in SI following the ramp conditions. Raman spectra, collected on a Renishaw InVia Confocal Raman microscope, are used to determine CNT crystallinity by employing the ratio of the peak intensities of the G and D bands (I_G/I_D) [30] with the 532 nm excitation laser wavelength. Spectra are collected at multiple spots for each sample and values are averaged to account for potential sample heterogeneity. CNT aspect ratio is determined by measuring the extensional viscosity of dilute solutions of CNTs in chlorosulfonic acid [31], enabling the measurement of an ensemble-averaged aspect ratio of CNTs (which correlate with the mechanical and electrical properties of fibers made from CNTs [6]). At least three measurements are performed for each sample, and the average values are reported. We obtain the CNT diameter distribution and CNT number of walls statistics using high-resolution transmission electron microscopy (HR-TEM) with an FEI Titan Themis [3] model at a 300 kV accelerating voltage, measuring 50 CNTs per sample. Nitrogen-carbon bonds in samples are detected by X-ray photoelectron spectroscopy (XPS) on a Thermo Scientific Nexsa G2 spectrometer, using monochromatic Al-Kα X-ray radiation (1.486.6 eV) with a selected spot size of 400 μm. The samples were analyzed with a spectra resolution of 0.100 eV at a constant analyzer pass energy of 20.000 eV. Three measurements are performed for each sample to account for heterogeneity in the surface composition. The data are analyzed and processed using Avantage software, where the atomic surface composition is calculated based on built-in sensitivity factors for different elements and peak areas after the Shirley background subtraction.

2.3. CFD simulation and reactor temperature profile measurement

To elucidate the phenomena within the reactor, we conduct CFD simulations using CatalyticFoam [32,33], a numerical framework capable of accurately solving the three-dimensional, time-dependent Navier-Stokes equations in conjunction with mass and energy balances. Simulations are done under the simplifying assumption of steady flow and non-reacting gases to approximate the baseline fluid mechanics and transport that occur in the absence of CNT synthesis. Note that this assumption is expected to capture reasonably well the fluid dynamics within the reactor before CNT growth starts. In most experimental conditions, growing CNTs form an aerogel that moves toward the end of the reactor. The presence of the aerogel likely affects the flow and temperature profiles; however, considering that the CNT volume fraction in the reactor is

$$\phi \approx \frac{\dot{m}_{CNT}}{\dot{m}_{gas}} \frac{\rho_{gas}}{\rho_{CNT}} \approx 10^{-7} \tag{3}$$

and could be about two orders of magnitude higher in the aerogel formation region, the fact that the aerogel appears to form at the interface of the jet and the forward-moving section of the vortex, we expect that the simulations should still capture the main flow features (e.g. recirculation vortex)—although the aerogel will undoubtedly affect the detailed flow features. This is consistent with the experimental observations that the aerogel moves along the reactor and that aerogel formation causes only minimal changes in the upstream reactor pressure (below 1 kPa, i.e., less than 1 % of the operating pressure). Most importantly, aerogel formation is unlikely to affect the relative flow features—i.e., shorter jet at lower injection Reynolds number. Additional details on the specific models are available in the SI.

The simulations are performed in a digital reconstruction of the FCCVD reactor. Information on the geometry reconstruction and mesh generation can be found in the SI. An experimentally measured static (no flow) temperature profile is applied as a boundary condition to the reactor wall, as depicted in SI Figure S3. The injection cannula is incorporated into the simulations as a zero-thickness thermal resistance layer, with a known thermal conductivity (based on ~20 W/m·K and thickness of 0.8 mm). Radiative heat transfer between the reactor walls and outer surface of injection cannula is considered using the finite volume discrete ordinate method, specifying the emissivity of the lateral walls and the outer surface of the cannula. Detailed boundary conditions and the simulation setup are also provided in the SI.

To provide boundary conditions to the CFD, wall temperature was measured via a thermocouple placed near the wall, as was done in previous works [23,24,34]. To minimize radiative effects, the thermocouple was enclosed in alumina shield (9.5 mm diameter) and coated with hBN. Measurements under both static and flowing conditions show minimal influence from convection. The measured temperature is within 5 °C range of the furnace zones setpoint (1200 °C) in the heated section, and the presence of flowing gas does not significantly alter the measured wall temperature profile (Fig. S4), indicating that heat conduction along the furnace wall and radiative coupling of opposing furnace walls dominate the wall temperature over convective heat exchange to the gas. Direct centerline temperature measurements were not conducted because inserting a shielded thermocouple in the injection cannula would alter the flow and transport to the point of preventing meaningful comparisons with CFD.

The injection temperature is the gas temperature at the exit of the injection cannula (values in SI Table S2), derived from CFD simulations, averaged across the cross section of the cannula. We used calculated temperature instead of direct measurements by thermocouple, because thermocouple placement inside the cannula would disrupt the fluid flow and change the temperature profiles inside the cannula. Moreover, radiative coupling of thermocouple with the reactor walls may cause significant deviations of measured value from the actual gas temperature. Hereafter, dimensionless numbers are calculated using the CFD derived injection temperature.

3. Results and discussion

3.1. Physical properties of process gases and key dimensionless numbers

Ar [35,36], N_2 [37,38], He [39], and H_2 [34,40] are common process gases utilized in the FCCVD CNT growth process. They serve multiple purposes, including carrying catalyst precursors into the reactor, diluting the reacting gases, controlling the residence time within the reactor (without changing the feedstock flow rate), and, in the case of H_2, controlling the decomposition of the precursors and feedstock. In our baseline process (a modification of Lee et al. [22] optimized to our reactor configuration), a binary process gas composition (H_2 and Ar) was used in addition to CH_4 as the carbon source. The simplest overall reaction to produce CNTs from CH_4 is

$$CH_4 \xrightarrow{\Delta \text{ and catalyst}} C_{CNT} + 2H_2 \tag{4}$$

Of course, a complex network of reactions occurs within FCCVD reactors and H_2 is an active process gas that directly participates in the CH_4-to-CNT reaction network. The presence of H_2 is known to inhibit CH_4 homogeneous pyrolysis by decreasing active carbon species formation rate and quenching the methyl radicals [41]. It can be beneficial in moderate amounts (increase CNT selectivity and quality by reducing competing non-catalytic or homogeneous reactions [3,14]) or harmful in excessive concentrations (impede the production of active carbon species required to initiate CNT growth and reduce productivity). Additionally, H_2 is known to have other chemical effects such as accelerating ferrocene decomposition [42] and etching of carbon impurities [43].

Although Ar is chemically inert and does not directly participate in reactions, its physical properties—such as density, thermal conductivity, and viscosity—can still impact CNT synthesis through heat, mass and momentum transfer effects. For instance, radial and axial thermal gradients in the reactor that may induce buoyancy-driven (thermo-convective) secondary flows that may impact reactor performance. H_2 influences the reaction environment not only through its chemical reactivity but also due to its own physical properties—it is much lighter, more thermally conductive, and less viscous compared to Ar. However, chemical and transport effects of H_2 cannot be disentangled directly. To address this, we use He: it shares similar physical properties with H_2 while also being chemically inert like Ar, allowing us to isolate and study the transport effects of H_2 without confounding chemical interactions. We also study the use of N_2 as an alternative to Ar; the physical properties of N_2 are very similar to Ar, though it could have some degree of reactivity at high temperatures (>1000 °C) of the FCCVD environment [44]. Later we show that N_2 does not react meaningfully at tested conditions (see section 3.3 and 3.4). Selecting these four gases allows rational design of reaction compositions where we develop a symmetry between higher molecular weight (Ar/N_2) and lower molecular weight (He/H_2) gases.

We employ dimensionless numbers to describe the transport phenomena inside the reactor. All physical properties are evaluated at the injection temperature. These injection temperatures are obtained from CFD simulations at the end of the cannula and are provided in SI Table S2. The Reynolds number (Re) (Equation (5)) represents the ratio of convective to diffusive momentum transfer; it is a fundamental parameter identifying the formation and spreading of the jet [45,46].

$$Re = \frac{4\dot{m}}{\pi d \mu\left(T_{inj}\right)} \tag{5}$$

where $\dot{m}$ is mass flow rate (obtained from MFC readings), d is the characteristic length (in our case, the injection cannula diameter), T_{inj} is gas temperature at the injection point, and μ is the dynamic viscosity of the injected gas mixture, estimated by Wilke's method (see Supplemental Information).

A lower Re indicates reduced influence of fluid inertial force, resulting in a faster dissipation of the injection jet. The Rayleigh number (Ra) (Equation (6)) – representing the time scale ratio for diffusion and convective heat transport – characterizes the buoyancy-driven convection in the reactor tube, which could interact with the injector jet and affect the heat transfer within the flow:

$$Ra = Gr \times Pr = \frac{g\beta\Delta T D^3}{\mu\left(T_{inj}\right)} \bullet \frac{c_p\left(T_{inj}\right)\rho\left(T_{inj}\right)^2}{k\left(T_{inj}\right)} \tag{6}$$

where g is the acceleration due to gravity, β is the gas volumetric thermal expansion coefficient, ΔT is the temperature difference between the reactor wall and gas at the outlet of the cannula, D is the characteristic length (in our case, the reactor diameter), c_p is the specific heat capacity at constant pressure, $\rho\left(T_{inj}\right)$ is the density, and $k\left(T_{inj}\right)$ is the thermal conductivity for gas mixture calculated at injection temperature. Ra is the product of the Grashof number (*Gr*), which measures the relative influence of buoyancy versus viscous forces, and the Prandtl number (Pr), which compares momentum diffusivity to thermal diffusivity. Higher Ra corresponds to stronger buoyant convection and may induce cross-stream secondary flows in the reactor tube [47]. Re and Ra calculations as well as additional dimensionless numbers are provided in the SI (see Table S2). Note that there are six additional independent geometrical dimensionless numbers (length of the furnace tube/inner diameter of the furnace tube; outside diameter of the cannula/inner diameter of the furnace tube; thickness of the cannula wall/diameter of the cannula; length of the cannula/inner diameter of the furnace tube; distance between the reactor flange and the first heated section/reactor tube diameter; length of heated section/reactor length) which are kept constant throughout this study. The effect of these parameters may play a role for intensifying the reaction (i.e., attaining a higher CNT productivity for the same gas flow rate) and determining scaling laws for DI reactors (i.e., accommodating higher gas flow rates by changing reactor size); however, this study cannot by itself provide guidance for scaleup because the reactor size and gas flow rates were not varied. Speculatively, if the size of the reaction zone is limited by mass transport across the interface between the jet and the recirculating gas (as discussed further), increasing the diameter of the reactor would only yield a linear increase in productivity (rather than quadratic, as would be expected when utilizing most of the reactor cross section); such scaling would be unfavorable for large-scale production of CNTs.

We start by analyzing changes in dimensionless numbers as a function of different degrees of Ar substitution by N_2, H_2, and He. Fig. 2 illustrates that substituting Ar by N_2 results in minimal changes to Re and Ra; therefore, we hypothesize that this replacement would not alter reaction performance. In contrast, substituting Ar by He leads to both lower Re and Ra. A similar effect is observed when Ar is substituted by H_2, but its reactivity should also be considered. In fact, through systematically choosing gas compositions, one can distinguish between transport and chemical (in the case of H_2) effects of the process gases on synthesis in terms of deep-injection FCCVD. At a given composition, we would expect H_2 and He to have nominally the same reaction performance if only transport effects are at play. Any significant difference we attribute to H_2 chemical effects when other process parameters are held constant.

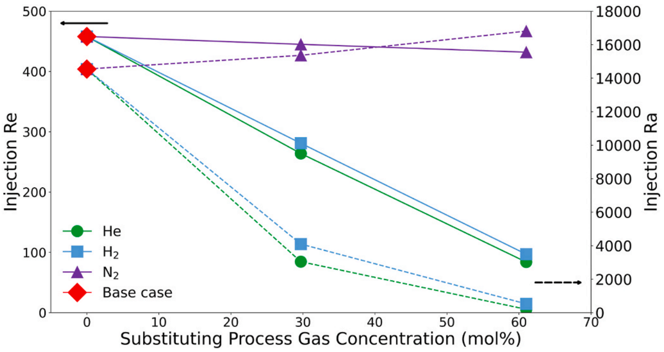

Fig. 2. Injection Reynolds number (Re) and Rayleigh number (Ra) as a function of substituting process gas concentration (concentration of H_2/He/N_2 replacing Ar in the baseline recipe). The solid line refers to injection Re and the dashed line refers to injection Ra. Injection Re/Ra is defined as the values at the injection point. Temperatures used to calculate Re and Ra were predicted by CFD for each condition. The baseline recipe is marked as a red diamond, corresponding to 0 % gas substitution. (For interpretation of the references to color in this figure legend, the reader is referred to the Web version of this article.)

3.2. *CFD study of process gas composition effects*

Based on our analysis of the dimensionless numbers, we conducted CNT growth experiments by substituting Ar with gradually changing amounts of He, H_2, or N_2 (Table 2 and detailed conditions in SI Table S1), supported with CFD simulations. Fig. 3a shows temperature and velocity maps for the baseline case, consisting of 2.5 % CH_4, 36.5 % H_2 and 61 % Ar (hereinafter, all concentrations are molar basis unless otherwise stated; results for other conditions can be found in SI Figure S5). The temperature map illustrates that the injected gas forms a jet that persists for several reactor diameters into the reactor, consistent with theoretical estimates for laminar jets [48] ($Re = 458$). This jet sets in motion a large axial recirculation that moves gases from the downstream sections to the upstream sections of the reactor. The jet also transports colder gas deep into the reactor's hot zone, creating a significant temperature difference between the jet and furnace walls. The jet tends to bend toward the bottom wall of the reactor due to the effects of the density gradient, which induces a secondary flow perpendicular to the reactor axis, driven by natural convection, more pronounced, characterized by high Ra (~14000). This secondary flow increases the radial mass flux towards the colder center of the reactor, including the cannula—in fact, the top wall of the cannula is about 100 K hotter than the bottom according to simulations. As the jet moves downstream and heats up, this cross-stream secondary flow diminishes. However, the two recirculation flows remain interconnected (the streamlines are not closed), creating an overall flow pattern that resembles two swirling flows occupying the symmetrical halves of the reactor (Fig. 3b). Representative pathlines, illustrating the movement of the jet within the reactor and the recirculation of reactor gases back to the front end, are presented for both velocity and temperature maps in SI Figure S7 for the baseline case.

The axial recirculating cell, depicted in blue, extends from the hot zone to the area upstream of the injection point. The high-velocity jet from the cannula (middle of the red zone) and the gas moving upstream in the axial recirculation (blue) demonstrate how heat and mass return to the reactor front before rejoining the central stream (outer portion of the red zone). This main recirculation, driven by the jet momentum conservation, couples with the secondary flow, driven by natural convection, leading to complex flow patterns within the reactor. Importantly, the axial recirculation transports heat upstream, heating both the gas within the injection tube and the external portion of the jet. Because of the cross-stream secondary flow, this effect is particularly pronounced on the top side of the cannula, while the bottom part remains in contact with much colder gas. Fig. 3a shows cross-sectional views of the

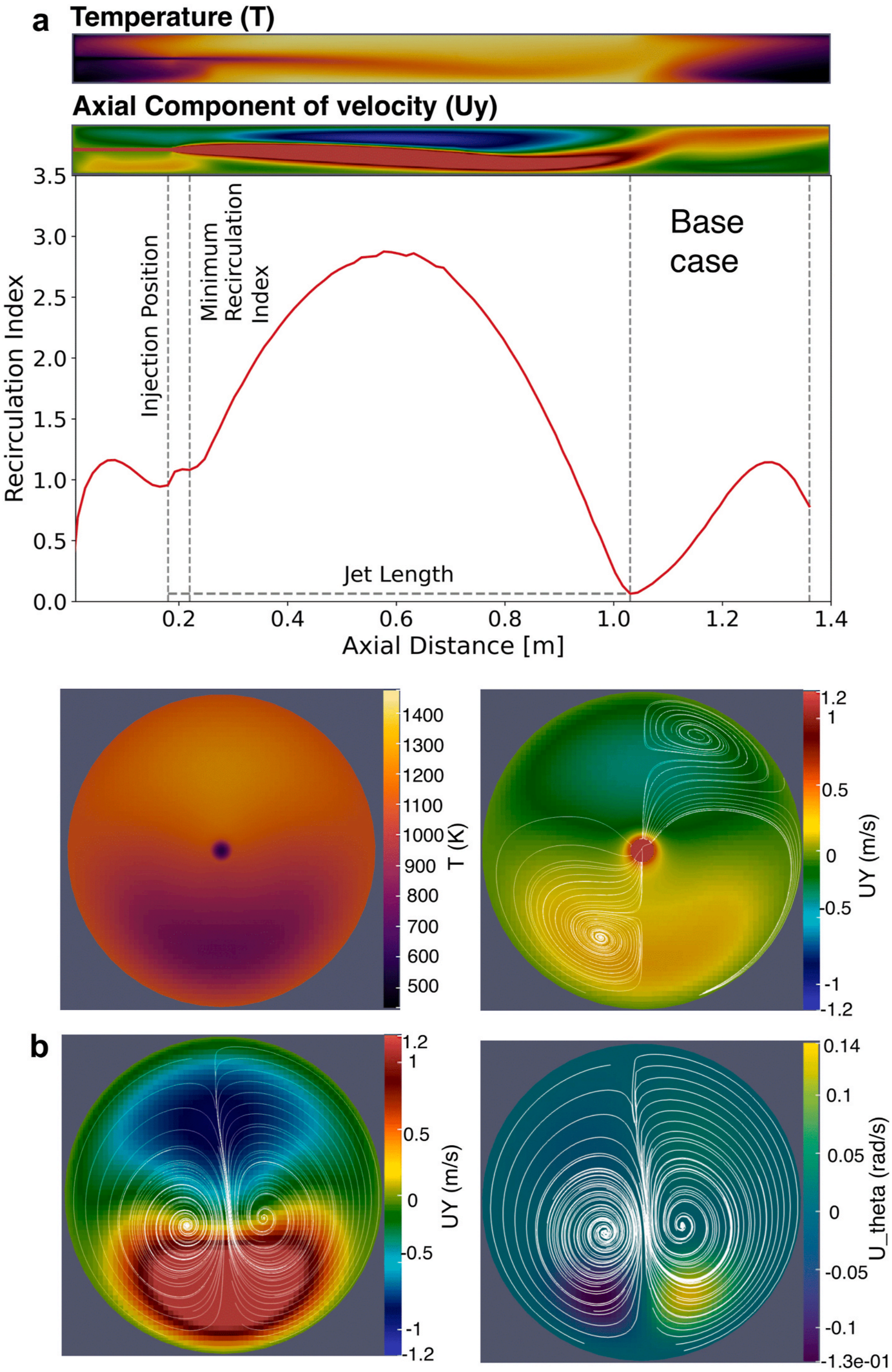

Fig. 3. (a) Temperature and velocity maps as well as calculated recirculation index as a function of reactor axial distance in a length of 1.36 m of the baseline case (61 % Ar). Cross-sections of the thermal and velocity maps at an injection depth of 18 cm are also included below. The velocity map is truncated at +1.2 m/s to highlight upstream flow regions, and the full velocity profile can be found in SI Figure S6. (b) Axial (left) and angular (right) velocity cross-sections at a depth of 80 cm in a 1.36 m reactor for the baseline case (61 % Ar, 36.5 % H_2, 2.5 % CH_4). Streamlines highlight two symmetric swirling flow regions occupying the reactor halves. The angular velocity map highlights rotational flow patterns of significantly lower magnitude than axial velocity, contributing to vortex formation and enhanced mixing.

temperature distribution at the injection plane, which highlights that both natural convection and radiation from the lateral walls to the cannula are important in establishing the overall temperature profile.

While color maps are useful for visualizing recirculation patterns in reactors, they provide only qualitative information. In a steady-state process, mass conservation dictates that the net mass flux across any plane perpendicular to the reactor axis, including the cross-section of the cannula, must equal the total inlet mass flow. Thus, any upstream mass flow is necessarily balanced by a downstream mass flow in addition to the flow arising from gas injection, which allows us to quantify the extent of recirculation by comparing the magnitude of the mass flow in the upstream direction to the injected mass flow, as shown in Equation (7). Hereinafter, we refer to this value as the recirculation index.

$$\text{Recirculation Index} = \frac{\dot{m}_{\text{upstream}}}{\dot{m}_{\text{injected}}} \tag{7}$$

We use the recirculation index to convert qualitative information from the color maps into a quantitative scalar value. When plotted along the reactor axial dimension, the recirculation index shows two distinct peaks, one upstream and one downstream of the injection point. The point of reduced recirculation (the minimum recirculation index) connects the upstream and downstream cells. The index also shows a single recirculation zone, with gas moving upstream from the downstream recirculating gas, not directly from the cannula. Changing gas composition moves the second recirculation peak upstream when Re is reduced, as the jet from the cannula penetrates shallower into the reactor. Despite this, the two main recirculation zones remain connected in all cases examined (SI Figure S5). Notably, the maximum strength of the recirculation (measured by the recirculation index) shows little change as Re is lowered—however, at lower Re the recirculation index decays rapidly to zero downstream the reactor. Moreover, the simulation shows that temperature difference between the top and bottom of the cannula is significant, meaning that recirculating gas effectively heats the top of the cannula.

3.3. *Effects of process gas composition on CNT growth yield and selectivity*

Fig. 4 presents the experimental results of CNT growth using different process gas compositions that range from enrichment in high-density gases (Ar and N_2) to compositions dominated by low-density gases (H_2 and He). Additionally, CFD velocity maps at selected concentrations (0 %, 30 %, 61 %) for each process gas type are shown to facilitate analysis. Fig. 4a shows that CH_4 to solid carbon conversion remains almost unchanged when Ar is replaced with N_2, even at complete substitution, meaning Ar and N_2 perform similarly due to their comparable physical properties. Since Re and Ra are nearly the same, the flow pattern for the 61 % N_2 case is similar to the baseline, with a jet length spanning the whole hot zone of the reactor. When Ar is substituted with lighter He (Fig. 4b), the recirculation shrinks in length due to lower Re, but does not affect the CH_4 to solid carbon conversion until the He concentration exceeds ~30 % (Re = 264); beyond this concentration, conversion starts dropping and reaches 5.1 % when Ar is fully substituted by He (Re = 84). Notably, Ra decreases concomitantly with the Re as the He concentration is increased; this leads to progressively weaker buoyancy-induced secondary flows and a more symmetric velocity profile. Substituting Ar with H_2 (Fig. 4c) causes an initial increase in conversion, peaking at 10 % H_2 substitution (46.5 % of total gas, Re = 393), followed by a rapid drop at higher H_2 contents. Because Re and Ra are nearly the same in the cases of He and H_2 substitution, we attribute the difference in conversion to chemical effects of increased H_2 concentration. In fact, at ~30 % substituting gas concentration, conversion is 11.1 % in the case of He and has dropped to 3.0 % in the case of H_2. Beyond this point, both transport effects and chemical effects lead to further decline in conversion, until it drops to 0.17 % at complete H_2 substitution (H_2/CH_4 input molar ratio ~40) which is a ~80x decrease from the highest CH_4 conversion (compared to a ~2x drop in the case of full He substitution). This much higher H_2/CH_4 ratio suppresses the conversion by inhibiting the formation of reactive carbon species, and the nature of the chemical effects of H_2 will be the subject of a future publication.

CFD simulations give further insights into experimental productivity. To interpret the velocity profiles quantitatively, the jet length is identified as the distance between injection point and the point where the recirculation index falls to zero (or near-zero), as demonstrated in Fig. 3a. Recirculation index plots and corresponding jet lengths for each process gas composition can be found in Supporting Information (see Fig. S5). The length of an isothermal, laminar jet expanding in a circular duct [48] can be estimated from Re:

$$l_{mix} \propto Re_{jet} D_{reactor} \tag{8}$$

The plot of jet length vs. $Re_{jet}D_{reactor}$ derived from CFD simulations is provided in SI Figure S8; although the jet is not isothermal, the calculated length follows Equation (8) (R^2 of 0.88).

The reduction in jet length is primarily due to the lower density of the gas resulting in a smaller momentum of the stream (see Fig. 5a) and is accompanied by smaller cross-stream buoyancy-induced secondary flows. According to our results higher conversion is observed for experimental conditions (carrier gas concentration) establishing profile with high length of the jet (Fig. 5b). In fact, reaction productivity in He substitution case is relatively unaffected by jet length when the jet is longer than ~0.45 m (corresponding to a Re of approximately 260), and the reaction drops with decreasing jet length, which correlates with Re falling below ~90, indicating a threshold nature of jet length effect.

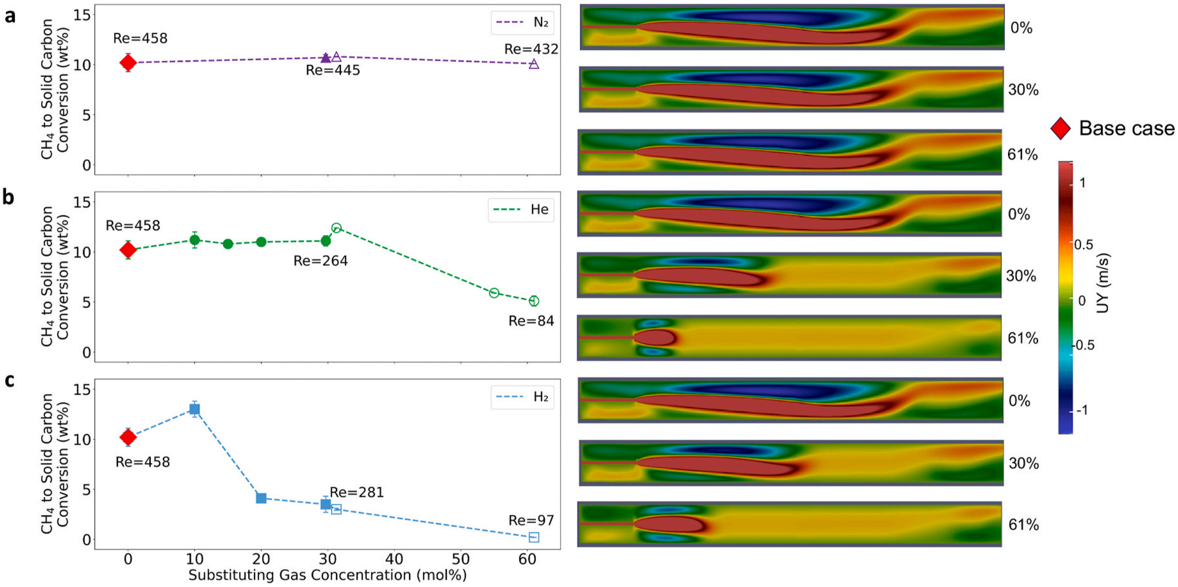

Fig. 4. CH_4 to solid carbon conversion as a function of substituting process gas concentration of (a) N_2, (b) He and (c) H_2 (H_2/CH_4 is changing). Velocity profiles at three selected concentrations (0 %, 30 %, 61 %) for each process gas are shown on the right. The velocity maps are truncated at +1.2 m/s to highlight upstream flow regions and the full velocity maps can be found in SI Figure S6. The baseline recipe is marked as a red diamond, corresponding to 0 % gas substitution. (For interpretation of the references to color in this figure legend, the reader is referred to the Web version of this article.)

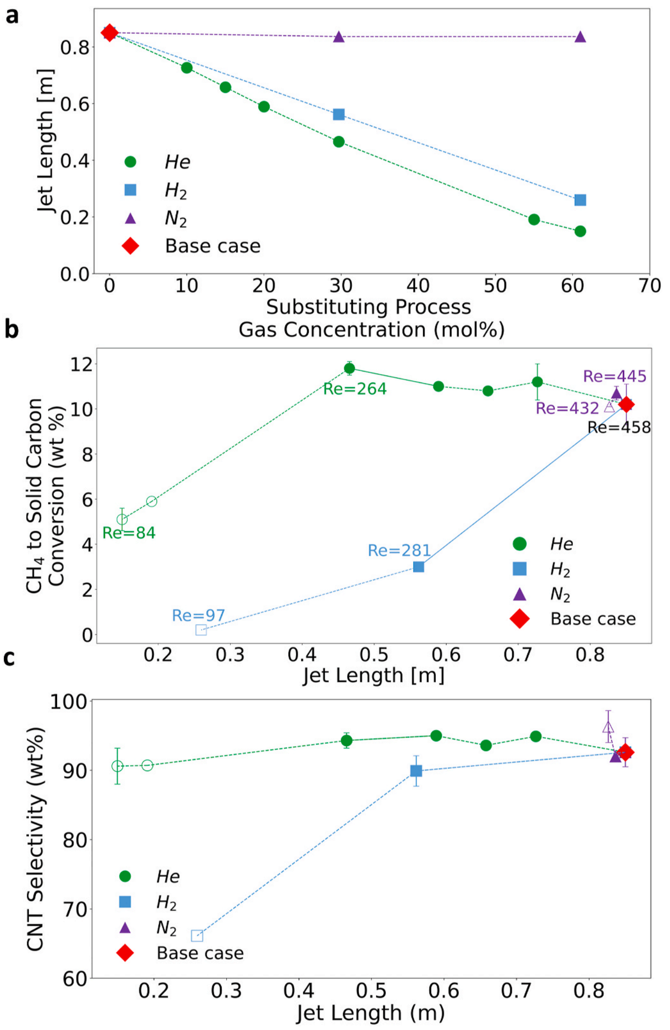

Fig. 5. (a) The jet lengths were extracted from the recirculation index and plotted as a function of substituting process gas concentration of N_2/He/H_2. (b) CH_4 to solid carbon conversion as a function of mixed jet length for different process gas types and composition conditions. (c) CNT selectivity as a function of mixed jet length for different process gas types and composition conditions. Substituting concentration refers to the concentration of N_2/He/H_2 to replace Ar in the baseline recipe. A filled mark indicates that Ar was used as a catalyst carrier while an empty mark indicates that the substituting gas was used (more details in SI can be found in SI). The baseline recipe is marked as a red diamond, corresponding to 0 % gas substitution. (For interpretation of the references to color in this figure legend, the reader is referred to the Web version of this article.)

When He is replaced with H_2, both chemical effects and transport phenomena come into play as H_2 concentration increases, leading to a negligible conversion at the total substitution of Ar. Conversely, the higher reaction yield observed under baseline and N_2 substitution conditions can be attributed to the longer jet. Therefore, our observations suggest that the jet length is the key factor influencing reaction conversion, with the reaction likely nearing completion by the time the flow reaches a critical length (might be shorter than the 0.45 m in 30 % He conditions). Based on these experiments and simulations, it is not possible to determine whether and how strongly conversion is influenced by the buoyancy-induced flows, which also bring heat from the lower reactor wall to the central reaction zone. These aspects could be studied by comparing horizontal and vertical reactors operating in the same conditions; this will be a matter of further research.

CNT selectivity (Fig. 5c) is maintained when Ar is replaced by N_2. Therefore, we find no measurable difference in the CNTs produced with Ar or N_2, indicating that N_2 does not participate in the reactions at these reactor conditions. We further confirm N_2 chemical inertness by XPS of the samples, which find no incorporation of N_2 in the CNTs (details can be found in SI Figure S9 and Table S3). Thus, we conclude that Ar and N_2 can be used interchangeably as inert process gases for CNT production at our reaction conditions. Unlike CH_4 conversion, we find that CNT selectivity is not strongly influenced by transport effects—in fact, high selectivity is maintained at a full replacement by He, even though conversion drops by a factor of two. However, chemical effects present at elevated H_2 content (where the H_2/CH_4 ratio is ~40) are important, as shown by the 27 % reduction in the percentage selectivity; likely, formation of active species is suppressed in the reactor zone where the catalyst particles reach their optimal size; in fact, we find high residual Fe percentage (81 %) in the collected material, which is consistent with a larger proportion of carbon-coated catalyst particles (TEM images can be found in Fig. S10).

Additionally, the effects of substituting different process gases on recirculation patterns are illustrated by the temperature profiles and cross-sections at the injection plane (Fig. 6a-c). Notably, temperatures above the injection cannula are higher with strong recirculation in Ar and N_2 cases due to their higher Ra, indicating a greater tendency for natural convection flows. These flows stir the gas, mixing hotter and cooler regions. Conversely, H_2 and He with lower Ra exhibit reduced convection flows, resulting in a more uniform temperature distribution across the cross-section as their concentration increases. This demonstrates how variations in natural convection (Ra) significantly influence recirculation and temperature distribution. The flow pattern also shows cross-stream recirculations caused by buoyancy, especially when

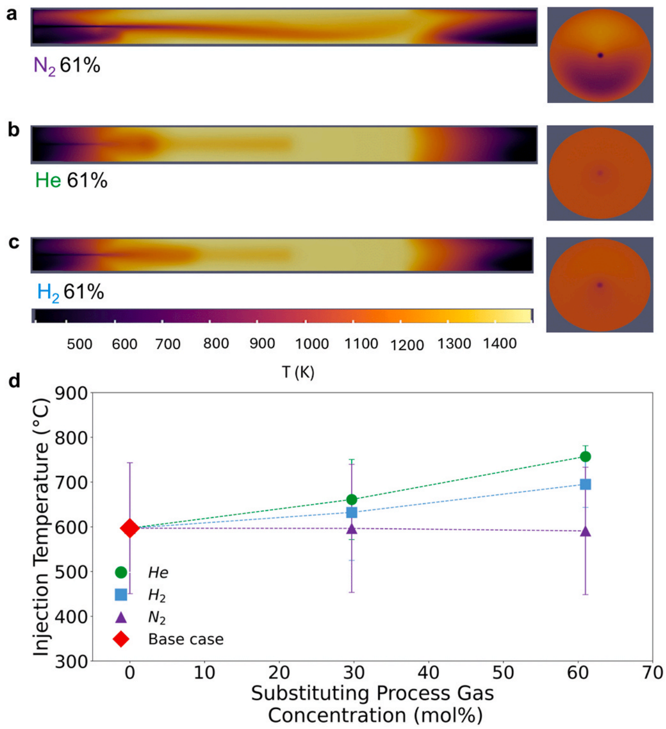

Fig. 6. Temperature maps for (a) a full replacement of Ar by N_2 (61 % N_2), (b) a full replacement of Ar with He (61 % He), and (c) a full replacement of Ar with H_2 (61 % H_2). A cross-section of the thermal map at an injection depth of 18 cm is also included in each case. (d) The mass-averaged temperature at the injection tube outlet with radiation incorporated as a function of substituting process gas concentration (concentration of H_2/He/N_2 replacing Ar in the baseline recipe). The injection depth is 18 cm, and the baseline recipe is marked as a red diamond corresponding to 0 % gas substitution. (For interpretation of the references to color in this figure legend, the reader is referred to the Web version of this article.)

changing gas composition. We cover a Ra range from ∼14000 to 17000 for baseline/full N_2 substitution cases, with a distinct feature of buoyancy-driven flow, to Ra∼200–500 for full He/H_2 substitution cases, with almost axially symmetric flow pattern. However, in our tested conditions, buoyancy effects are suppressed only within the conditions that provide low reaction outcomes due to decreased jet length. Videos of the forming catalyst particle cloud (which serve as flow tracers) are consistent with the CFD simulations showing a collimated jet that bends downward in the middle of the reactor, splits into two lobes, and turns upward closer to the end of the heated zone at high Re & Ra, vs. a relatively uniform flow profile across the reactor cross section at low Re & Ra (Fig. S12).

It is worth mentioning that in CFD simulations, we also examine the thermal environment within the injection cannula, as it may serve to preheat the process gases. Fig. 6d shows the temperature inside the cannula at the injection point, for various process gas types and compositions. Simulations are run with radiative heat transfer from the reactor walls to the cannula and gives ∼200 °C higher gas temperature at the end of the injection cannula, compared to case without radiative (gas temperature without radiation incorporated can be found in SI Figure S13). Therefore, the injection tube operates as a preheater, which not only bypasses the thermal gradient at the front end but also raises reactant temperatures when exposed to the hot zone, and this preheating mechanism might beneficially contribute to synthesis efficiency in the deep injection method.

We find that injection temperatures depend on process gas conditions and might influence reaction productivity. The highest temperature observed is for the 61 % He case, with a gas temperature at the end of the injection tube reaching 757 °C, about 160 °C higher than the base case at 597 °C, according to CFD simulations. The 61 % He case yields a ∼2x drop in conversion compared to the baseline case, which could be due to excessively high injection temperature as observed in the original DI-FCCVD process [22]. To check whether the lower conversion is due to higher injection temperature, shorter jet length, or both, we run experiments using the base case gas composition and a deeper injection to have a higher injection temperature; we find that CH_4 to solid carbon conversion improved with injection temperature in the baseline conditions, 13 % increase at 707 °C and 36 % increase at 812 °C, while CNT selectivity is maintained (data can be found in SI Figure S14). Therefore, it appears that the drop in conversion in the He case is due to a shorter jet length rather than a higher injection temperature.

3.4. Effects of process gas composition on CNT quality

We examine the effects of process gas type and composition on CNT quality using Raman I_G/I_D ratio (to index crystallinity) and aspect ratio as key metrics because these factors govern solution-spun CNT fiber properties. Fig. 7a-b shows Raman I_G/I_D ratios at 532 nm laser wavelength and Fig. 7c-d presents aspect ratios of purified samples (CNTs) from selected growth conditions. The quality of produced CNTs generally follows the same trends as the CH_4 to solid carbon conversion: high crystallinity (Raman I_G/I_D ratio ∼90–110 at 532 nm) and high aspect ratio (above 6000) are obtained when conversion is above ∼10 %, whereas lower crystallinity (below 50 at 532 nm) and lower aspect ratio (below 3000) are measured when conversion falls below 5 %. Because the measured aspect ratio changes range from 2000 to 11000, the synthesized FWCNTs would yield fibers in a broad range of strength and electrical conductivities—in addition to being synthesized at various productivities [6]. Therefore, across a broad range of conditions, deep-injection FCCVD can simultaneously yield high CNT conversion and high CNT quality, which may seem unexpected (usually higher CNT productivity is accompanied by a drop in quality [49]). TEM analysis of the samples (SI Figure S15), produced at different gas compositions, reveals that most of CNTs are single- and double-walled. More details on CNT diameter, aspect ratio and wall number can be found in SI (Table S4). N_2 is also found to be interchangeable with Ar when reactor productivity and product quality metrics are considered. Beyond the fundamental point, the interchangeability of Ar with N_2 as an inert process gas is important for economic and sustainable reasons because N_2 has significantly lower embodied energy (44x lower than Ar on a molar basis [50]), higher abundance and much lower cost, all favorable in production scaling.

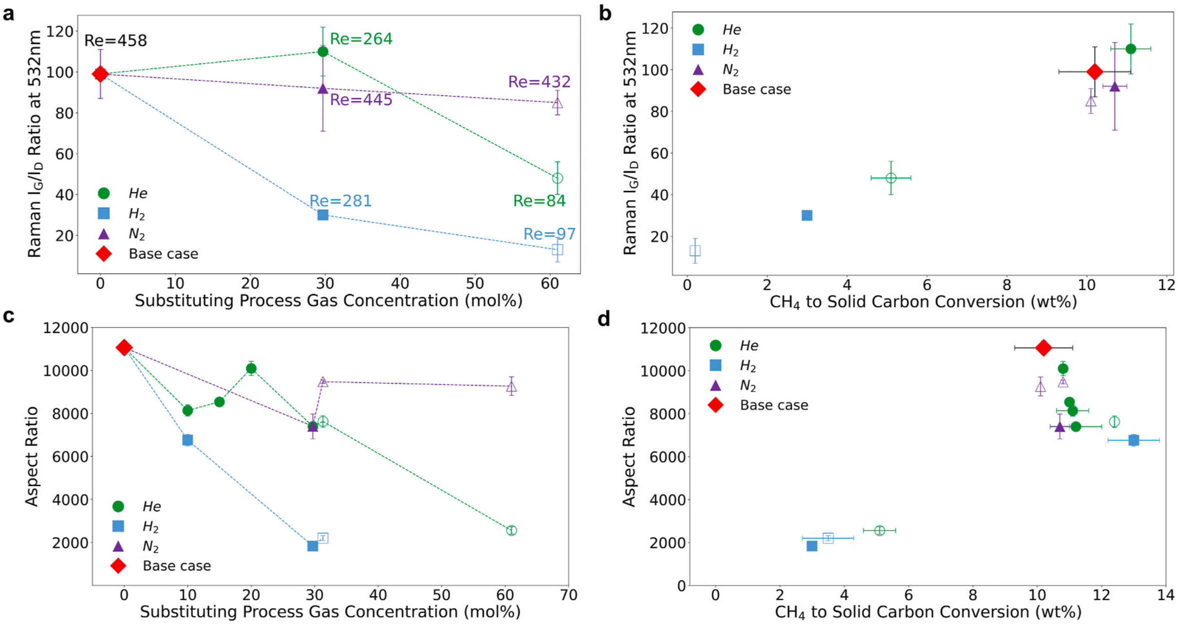

Fig. 7. (a) Raman I_G/I_D ratio at 532 nm as well as (c) aspect ratio of purified samples as a function of substituting process gas concentration (concentration of H_2/He/N_2 replacing Ar in the baseline recipe). (b) Raman I_G/I_D ratio at 532 nm and (d) aspect ratio of purified samples as a function of CH_4 to solid carbon conversion for better illustration. In (c–d), the measurement of aspect ratio from 61 % H_2 condition is lacking due to a limited purified sample size from an extremely low productivity. A filled mark indicates that Ar is used as a catalyst carrier while an empty mark indicates that the substituting gas is used. The baseline recipe is marked as a red diamond, corresponding to 0 % gas substitution. (For interpretation of the references to color in this figure legend, the reader is referred to the Web version of this article.)

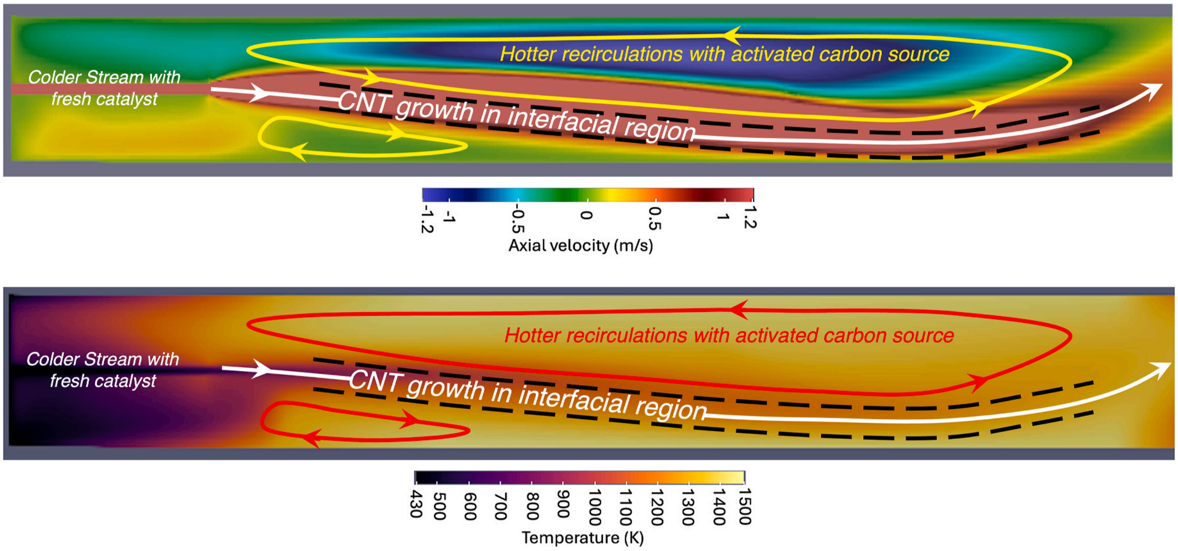

Fig. 8. Scheme of suggested mechanism of DI FCCVD reactor.

3.5. *Mechanism of deep injection reactor*

As discussed in section 3.3, the most productive synthesis conditions correspond to flow profiles with higher jet length. Thus, we propose the following mechanism of DI FCCVD synthesis (Fig. 8). We infer that CNT growth occurs at the interface between the colder jet containing freshly injected catalyst and hotter co-flowing recirculating gas, containing the activated carbon source. This leads to the “right sequencing” of catalyst formation and carbon feedstock activation, essential for FCCVD CNT growth. A sufficiently long jet may be necessary to provide enough reaction surface area at higher temperatures, explaining the presence of threshold jet length value (see Fig. 5b). However, more evidence is needed to arrive at a definitive mechanism.

4. Conclusion

We studied the effects of transport phenomena and chemical composition on a performance of deep injection FCCVD reactor by a process gas study, achieving CH_4 conversion of 13 %. We control independently transport and chemical effects by using N_2 and He as substituting process gases, beyond the original Ar and H_2, used in the baseline recipe. We find that a complete substitution of Ar by N_2 does not lead to noticeable changes in material yield and quality, which is attributed to their comparable physical properties and inertness. Notably, using N_2 instead of Ar enables a more sustainable and economically viable synthesis process. Conversely, reaction performance drops off when He or H_2 becomes a principal component of a process gas mixture, likely because the jet length becomes shorter due to the lower density of He and H_2. We also show that H_2 concentration has a drastic impact on reaction productivity due to a combination of chemical and transport effects. We believe these results provide useful considerations for further scale-up and intensification of the deep-injection method.

Furthermore, based on both experimental and computational indications, we propose an extended mechanism of deep-injection synthesis, showing that the use of an injection tube not only helps bypass the front recirculation zone but radiatively pairs with the reactor wall, serving as an efficient pre-heater and impacting the thermal environment throughout the reactor. A central recirculation is driven by the gas jet emerging from the cannula, transporting hot gas from the downstream portion of the reactor upstream and keeping the reactor walls clean. This central recirculation flow is crucial for achieving high reaction productivity, as CNT growth is expected to occur primarily at the interface between the cooler feed gas (containing the catalyst precursor) and the hotter recirculating gas enriched with activated carbon species (presumably C_2 compounds). These insights underscore the complex interplay between coupled chemical reactions, thermal dynamics, and flow patterns within the reactor, which could pose challenges to further intensification of this reactor configuration while also offering guidance for designing more efficient reactors in the future.

CRediT authorship contribution statement

Muxiao Li: Writing – review & editing, Writing – original draft, Validation, Methodology, Investigation, Conceptualization. **Jui Junnarkar:** Writing – review & editing, Writing – original draft, Software, Investigation, Formal analysis. **Arthur W.N. Sloan:** Writing – review & editing, Software, Methodology, Formal analysis. **Eldar Khabushev:** Writing – review & editing, Visualization. **Ana Victoria Benavides-Figueroa:** Writing – review & editing, Investigation. **Mingrui L. Gong:** Writing – review & editing, Investigation. **Miguel Garza:** Writing – review & editing, Investigation. **Joe F. Khoury:** Writing – review & editing, Investigation. **Davide Cavuto:** Writing – review & editing, Investigation. **Steven M. Williams:** Conceptualization. **Daniele Micale:** Writing – review & editing, Validation, Software, Methodology, Conceptualization. **Mauro Bracconi:** Writing – review & editing, Validation, Supervision, Software, Methodology, Formal analysis, Conceptualization. **Matteo Maestri:** Writing – review & editing, Supervision, Resources, Project administration, Funding acquisition, Formal analysis, Conceptualization. **Glen C. Irvin:** Writing – review & editing, Supervision, Project administration, Formal analysis, Conceptualization. **Matteo Pasquali:** Writing – review & editing, Supervision, Resources, Project administration, Funding acquisition, Formal analysis, Conceptualization.

Declaration of competing interest

The authors declare the following financial interests/personal relationships which may be considered as potential competing interests: Matteo Pasquali reports a relationship with Dexmat, Inc that includes: consulting or advisory and equity or stocks. If there are other authors, they declare that they have no known competing financial interests or personal relationships that could have appeared to influence the work reported in this paper.

Acknowledgments

We thank Leonardo Spanu, Robert Headrick, John Lockemeyer, Carl Mesters, Jack Lewnard, Marc von Keitz, Max Lyubovsky, and Dan Hancu for valuable discussions and suggestions. We thank S. M. Kim and his research group (KIST) for discussions and valuable assistance in reproducing their Deep Injection work and Adam Boies, Alan Windle, and their research collaborators (University of Cambridge) for valuable discussions and for sharing their design of a gas exchange valve at the reactor exit. This work was funded by Advanced Research Projects Agency-Energy Grant DE-AR0001015, Shell International Exploration & Production, Inc., the Robert A. Welch Foundation Grant C-1668, The Kavli Foundation Exploration Award in Nanoscience for Sustainability LS-2023-GR-51-2857, and the Carbon Hub. Part of this work was supported by the Novo Nordisk Foundation CO2 Research Center (CORC) with grant number NNF21SA0072700 and is published under the number CORC_24_34. CFD simulations were executed on the Rice Night Owls Time-Sharing (NOTS) high-performance computing cluster at Rice University's Center for Research Computing (CRC), funded by NSF grant CNS-1338099. The work was done in part using resources of the Shared Equipment Authority at Rice University. Muxiao Li and Jui Junnarkar acknowledge Shell Carbon Hub fellowships and Arthur W. N. Sloan acknowledges NASA Space Technology Research Fellowship Grant # 80NSSC18K1172. Matteo Maestri and Mauro Bracconi acknowledge funding from the National Recovery and Resilience Plan (NRRP), Mission 4 Component 2 Investment 1.3—Call for tender No. 1561 of 11. 10.2022 of Ministero dell'Università e della Ricerca (MUR); funded by the European Union – NextGenerationEU - Award Number: Project code PE0000021, Concession Decree No. 1561 of 11. 10.2022 adopted by Ministero dell'Università e della Ricerca (MUR), CUP D43C22003090001, according to attachment E of Decree No. 1561/ 2022, Project title "Network 4 Energy Sustainable Transition—NEST".

Appendix A. Supplementary data

Supplementary data to this article can be found online at https://doi.org/10.1016/j.carbon.2025.120259.

References

[1] M.F.L. De Volder, S.H. Tawfick, R.H. Baughman, A.J. Hart, Carbon nanotubes: present and future commercial applications, Science 339 (6119) (2013) 535–539, https://doi.org/10.1126/science.1222453.

[2] P. Hou, F. Zhang, L. Zhang, C. Liu, H. Cheng, Synthesis of carbon nanotubes by floating catalyst chemical vapor deposition and their applications, Adv Funct Materials 32 (11) (2022) 2108541, https://doi.org/10.1002/adfm.202108541.

[3] Y.-L. Li, I.A. Kinloch, A.H. Windle, Direct spinning of carbon nanotube fibers from chemical vapor deposition synthesis, Science 304 (5668) (2004) 276–278, https://doi.org/10.1126/science.1094982.

[4] B. Mas, B. Alemán, I. Dopico, I. Martin-Bragado, T. Naranjo, E.M. Pérez, J. J. Vilatela, Group 16 elements control the synthesis of continuous fibers of carbon nanotubes, Carbon 101 (2016) 458–464, https://doi.org/10.1016/j.carbon.2016.02.005.

[5] S.-H. Lee, J. Park, S.Y. Moon, S.Y. Lee, S.M. Kim, Strong and highly conductive carbon nanotube fibers as conducting wires for wearable electronics, ACS Appl. Nano Mater. 4 (4) (2021) 3833–3842, https://doi.org/10.1021/acsanm.1c00248.

[6] D.E. Tsentalovich, R.J. Headrick, F. Mirri, J. Hao, N. Behabtu, C.C. Young, M. Pasquali, Influence of carbon nanotube characteristics on macroscopic fiber properties, ACS Appl. Mater. Interfaces 9 (41) (2017) 36189–36198, https://doi.org/10.1021/acsami.7b10968.

[7] L.W. Taylor, O.S. Dewey, R.J. Headrick, N. Komatsu, N.M. Peraca, G. Wehmeyer, J. Kono, M. Pasquali, Improved properties, increased production, and the path to broad adoption of carbon nanotube fibers, Carbon 171 (2021) 689–694, https://doi.org/10.1016/j.carbon.2020.07.058.

[8] W. Ma, L. Song, R. Yang, T. Zhang, Y. Zhao, L. Sun, Y. Ren, D. Liu, L. Liu, J. Shen, Z. Zhang, Y. Xiang, W. Zhou, S. Xie, Directly synthesized strong, highly conducting, transparent single-walled carbon nanotube films, Nano Lett. 7 (8) (2007) 2307–2311, https://doi.org/10.1021/nl070915c.

[9] A.G. Nasibulin, A. Kaskela, K. Mustonen, A.S. Anisimov, V. Ruiz, S. Kivistö, S. Rackauskas, M.Y. Timmermans, M. Pudas, B. Aitchison, M. Kauppinen, D. P. Brown, O.G. Okhotnikov, E.I. Kauppinen, Multifunctional free-standing single-walled carbon nanotube films, ACS Nano 5 (4) (2011) 3214–3221, https://doi.org/10.1021/nn200338r.

[10] A. Kaskela, A.G. Nasibulin, M.Y. Timmermans, B. Aitchison, A. Papadimitratos, Y. Tian, Z. Zhu, H. Jiang, D.P. Brown, A. Zakhidov, E.I. Kauppinen, Aerosol-synthesized SWCNT networks with tunable conductivity and transparency by a dry transfer technique, Nano Lett. 10 (11) (2010) 4349–4355, https://doi.org/10.1021/nl101680s.

[11] F. Mirri, A.W.K. Ma, T.T. Hsu, N. Behabtu, S.L. Eichmann, C.C. Young, D. E. Tsentalovich, M. Pasquali, High-performance carbon nanotube transparent conductive films by scalable dip coating, ACS Nano 6 (11) (2012) 9737–9744, https://doi.org/10.1021/nn303201g.

[12] Q. Zhang, W. Zhou, X. Xia, K. Li, N. Zhang, Y. Wang, Z. Xiao, Q. Fan, E. I. Kauppinen, S. Xie, Transparent and freestanding single-walled carbon nanotube films synthesized directly and continuously via a blown aerosol technique, Adv. Mater. 32 (39) (2020) 2004277, https://doi.org/10.1002/adma.202004277.

[13] X. Gui, J. Wei, K. Wang, A. Cao, H. Zhu, Y. Jia, Q. Shu, D. Wu, Carbon nanotube sponges, Adv. Mater. 22 (5) (2010) 617–621, https://doi.org/10.1002/adma.200902986.

[14] M. Sehrawat, M. Rani, S. Sharma, S. Bharadwaj, B.G. Falzon, B.P. Singh, Floating catalyst chemical vapour deposition (FCCVD) for direct spinning of CNT aerogel: a review, Carbon 219 (2024) 118747, https://doi.org/10.1016/j.carbon.2023.118747.

[15] L. Zheng, Advanced materials primer. Carbon Nanotubes; BloombergNEF, 2021.

[16] L. Weller, F.R. Smail, J.A. Elliott, A.H. Windle, A.M. Boies, S. Hochgreb, Mapping the parameter Space for direct-spun carbon nanotube aerogels, Carbon 146 (2019) 789–812, https://doi.org/10.1016/j.carbon.2019.01.091.

[17] M.R. Predtechenskiy, METHOD AND APPARATUS FOR PRODUCING CARBON NANOSTRUCTURES, US 2020/0239316 A1, 2020.

[18] T. Saito, S. Ohshima, T. Okazaki, S. Ohmori, M. Yumura, S. Iijima, Selective diameter control of single-walled carbon nanotubes in the gas-phase synthesis, j nanosci nanotechnol 8 (11) (2008) 6153–6157, https://doi.org/10.1166/jnn.2008.SW23.

[19] C. Hoecker, F. Smail, M. Bajada, M. Pick, A. Boies, Catalyst nanoparticle growth dynamics and their influence on product morphology in a CVD process for continuous carbon nanotube synthesis, Carbon 96 (2016) 116–124, https://doi.org/10.1016/j.carbon.2015.09.050.

[20] A.G. Nasibulin, P.V. Pikhitsa, H. Jiang, E.I. Kauppinen, Correlation between catalyst particle and single-walled carbon nanotube diameters, Carbon 43 (11) (2005) 2251–2257, https://doi.org/10.1016/j.carbon.2005.03.048.

[21] F. Yang, H. Zhao, R. Li, Q. Liu, X. Zhang, X. Bai, R. Wang, Y. Li, Growth modes of single-walled carbon nanotubes on catalysts, Sci. Adv. 8 (41) (2022) eabq0794, https://doi.org/10.1126/sciadv.abq0794.

[22] S.-H. Lee, J. Park, J.H. Park, D.-M. Lee, A. Lee, S.Y. Moon, S.Y. Lee, H.S. Jeong, S. M. Kim, Deep-injection floating-catalyst chemical vapor deposition to continuously synthesize carbon nanotubes with high aspect ratio and high crystallinity, Carbon 173 (2021) 901–909, https://doi.org/10.1016/j.carbon.2020.11.065.

[23] G. Hou, R. Su, A. Wang, V. Ng, W. Li, Y. Song, L. Zhang, M. Sundaram, V. Shanov, D. Mast, D. Lashmore, M. Schulz, Y. Liu, The effect of a convection vortex on sock formation in the floating catalyst method for carbon nanotube synthesis, Carbon 102 (2016) 513–519, https://doi.org/10.1016/j.carbon.2016.02.087.

[24] A.G. Nasibulin, A. Moisala, D.P. Brown, H. Jiang, E.I. Kauppinen, A novel aerosol method for single walled carbon nanotube synthesis, Chem. Phys. Lett. 402 (1–3) (2005) 227–232, https://doi.org/10.1016/j.cplett.2004.12.040.

[25] S.Y. Moon, B.R. Kim, C.W. Park, S.-H. Lee, S.M. Kim, High-crystallinity single-walled carbon nanotube aerogel growth: understanding the real-time catalytic decomposition reaction through floating catalyst chemical vapor deposition, Chemical Engineering Journal Advances 10 (2022) 100261, https://doi.org/10.1016/j.ceja.2022.100261.

[26] I.W. Chiang, B.E. Brinson, A.Y. Huang, P.A. Willis, M.J. Bronikowski, J. L. Margrave, R.E. Smalley, R.H. Hauge, Purification and characterization of single-wall carbon nanotubes (SWNTs) obtained from the gas-phase decomposition of CO (HiPco process), J. Phys. Chem. B 105 (35) (2001) 8297–8301, https://doi.org/10.1021/jp0114891.

[27] Wang, H. Shan, R.H. Hauge, M. Pasquali, R.E. Smalley, A highly selective, one-pot purification method for single-walled carbon nanotubes, J. Phys. Chem. B 111 (6) (2007) 1249–1252, https://doi.org/10.1021/jp068229+.

[28] L.W. Taylor, O.S. Dewey, E.G. Biggers, M. Durán-Chaves, J.F. Khoury, M. Pasquali, Purification of carbon nanotubes for dissolution in chlorosulfonic acid, Carbon 228 (2024) 119317, https://doi.org/10.1016/j.carbon.2024.119317.

[29] V.A. Davis, A.N.G. Parra-Vasquez, M.J. Green, P.K. Rai, N. Behabtu, V. Prieto, R. D. Booker, J. Schmidt, E. Kesselman, W. Zhou, H. Fan, W.W. Adams, R.H. Hauge, J. E. Fischer, Y. Cohen, Y. Talmon, R.E. Smalley, M. Pasquali, True solutions of single-walled carbon nanotubes for assembly into macroscopic materials, Nature Nanotech 4 (12) (2009) 830–834, https://doi.org/10.1038/nnano.2009.302.

[30] M.S. Dresselhaus, G. Dresselhaus, R. Saito, A. Jorio, Raman spectroscopy of carbon nanotubes, Phys. Rep. 409 (2) (2005) 47–99, https://doi.org/10.1016/j.physrep.2004.10.006.

[31] D.E. Tsentalovich, A.W.K. Ma, J.A. Lee, N. Behabtu, E.A. Bengio, A. Choi, J. Hao, Y. Luo, R.J. Headrick, M.J. Green, Y. Talmon, M. Pasquali, Relationship of extensional viscosity and liquid crystalline transition to length distribution in carbon nanotube solutions, Macromolecules 49 (2) (2016) 681–689, https://doi.org/10.1021/acs.macromol.5b02054.

[32] D. Micale, C. Ferroni, R. Uglietti, M. Bracconi, M. Maestri, Computational fluid dynamics of reacting flows at surfaces: methodologies and applications, Chem. Ing. Tech. 94 (5) (2022) 634–651, https://doi.org/10.1002/cite.202100196.

[33] M. Maestri, A. Cuoci, Coupling CFD with detailed microkinetic modeling in heterogeneous catalysis, Chem. Eng. Sci. 96 (2013) 106–117, https://doi.org/10.1016/j.ces.2013.03.048.

[34] T. Fujimori, D. Yamashita, Y. Kishibe, M. Sakai, H. Inoue, T. Onoki, J. Otsuka, D. Tanioka, T. Hikata, S. Okubo, K. Akada, J. Fujita, One step fabrication of aligned carbon nanotubes using gas rectifier, Sci. Rep. 12 (1) (2022) 1285, https://doi.org/10.1038/s41598-022-05297-6.

[35] L. Ci, S. Xie, D. Tang, X. Yan, Y. Li, Z. Liu, X. Zou, W. Zhou, G. Wang, Controllable growth of single wall carbon nanotubes by pyrolizing acetylene on the floating iron catalysts, Chem. Phys. Lett. 349 (3–4) (2001) 191–195, https://doi.org/10.1016/S0009-2614(01)01098-3.

[36] L. Ci, Z. Rao, Z. Zhou, D. Tang, X. Yan, Y. Liang, D. Liu, H. Yuan, W. Zhou, G. Wang, W. Liu, S. Xie, Double wall carbon nanotubes promoted by sulfur in a floating iron catalyst CVD system, Chem. Phys. Lett. 359 (1–2) (2002) 63–67, https://doi.org/10.1016/S0009-2614(02)00600-0.

[37] E.-X. Ding, A. Hussain, S. Ahmad, Q. Zhang, Y. Liao, H. Jiang, E.I. Kauppinen, High-performance transparent conducting films of long single-walled carbon nanotubes synthesized from toluene alone, Nano Res. 13 (1) (2020) 112–120, https://doi.org/10.1007/s12274-019-2581-7.

[38] Z. Zhang, H. Dong, Y. Liao, E.-X. Ding, L. Lv, H. Li, J. Yan, E.I. Kauppinen, Dry-transferred single-walled carbon nanotube thin films for flexible and transparent heaters, Surf. Interfaces 31 (2022) 101992, https://doi.org/10.1016/j.surfin.2022.101992.

[39] P.-X. Hou, W.-S. Li, S.-Y. Zhao, G.-X. Li, C. Shi, C. Liu, H.-M. Cheng, Preparation of metallic single-wall carbon nanotubes by selective etching, ACS Nano 8 (7) (2014) 7156–7162, https://doi.org/10.1021/nn502120k.

[40] T. Saito, W.-C. Xu, S. Ohshima, H. Ago, M. Yumura, S. Iijima, Supramolecular catalysts for the gas-phase synthesis of single-walled carbon nanotubes, J. Phys. Chem. B 110 (12) (2006) 5849–5853, https://doi.org/10.1021/jp057513i.

[41] O. Olsvik, O.A. Rokstad, A. Holmen, Pyrolysis of methane in the presence of hydrogen, Chem. Eng. Technol. 18 (5) (1995) 349–358, https://doi.org/10.1002/ceat.270180510.

[42] J. Lei, K.V. Bets, E.S. Penev, B.I. Yakobson, Floating Fe catalyst formation and effects of hydrogen environment in the growth of carbon nanotubes, J. Phys. Chem. Lett. 14 (18) (2023) 4266–4272, https://doi.org/10.1021/acs.jpclett.3c00716.

[43] P.-X. Hou, B. Yu, Y. Su, C. Shi, L.-L. Zhang, C. Liu, S. Li, J.-H. Du, H.-M. Cheng, Double-wall carbon nanotube transparent conductive films with excellent performance, J. Mater. Chem. A 2 (4) (2014) 1159–1164, https://doi.org/10.1039/C3TA13685J.

[44] R. Alexander, A. Kaushal, A. Das, J. Bahadur, K. Dasgupta, Does carrier gas have a role on the yield and alignment of CNT fibers, Diam. Relat. Mater. 129 (2022) 109395, https://doi.org/10.1016/j.diamond.2022.109395.

[45] J.H.W. Lee, V.H. Chu, Turbulent Jets and Plumes, Springer US, Boston, MA, 2003, https://doi.org/10.1007/978-1-4615-0407-8.

[46] O. Levenspiel, Chemical Reaction Engineering, third ed., Wiley, New York, 1999.

[47] Frank P. Incropera, David P. DeWitt, Fundamentals of Heat and Mass Transfer, John Wiley & Sons, 2002.

[48] A. Revuelta, A.L. Sánchez, A. Liñán, Confined axisymmetric laminar jets with large expansion ratios, J. Fluid Mech. 456 (2002) 319–352, https://doi.org/10.1017/S0022112001007601.

[49] M.W.J. Glerum, A.M. Boies, Reactor processes for value added carbon synthesis and turquoise hydrogen, in: Advances in Chemical Engineering, vol. 61, Elsevier, 2023, pp. 133–192, https://doi.org/10.1016/bs.ache.2023.04.001.

[50] G. Weir, T. Muneer, Energy and environmental impact analysis of double-glazed windows, Energy Convers. Manag. 39 (3–4) (1998) 243–256, https://doi.org/10.1016/S0196-8904(96)00191-4.